JTTEE5 18:858–874
DOI: 10.1007/s11666-009-9395-1
1059-9630/$19.00 © ASM International

Peer Reviewed

Numerical Study of the Plasma Flow Field and Particle In-flight Behavior with the Obstruction of a Curved Substrate

Te Ba, Chang Wei Kang, and Heong Wah Ng

(Submitted January 30, 2009; in revised form July 8, 2009)

A three-dimensional numerical model is developed using computational fluid dynamics software FLUENT v6.3.26 to investigate the influence of curved substrate on the plasma flow fields and subsequent in-flight particle behavior. The curved substrates have two different dimensional shapes and are positioned in two orientations (convex or concave). It is found that inclusion of the substrates with different shapes in different directions significantly affects the plasma flow fields at the vicinity of the substrate, although the most upstream region of the plasma field remains unaffected. Plasma temperature and velocity contours and flow vectors in the computational domain, especially at regions near substrates are presented. Investigations on the size effect on the in-flight particle parameters are carried out, which show that smaller particles tend to acquire higher velocities and temperatures. Moreover, smaller particles are more susceptible to the flow change by the substrate inclusion. However, for the size range of the zirconia feedstock we used later, there is no obvious effect of the substrate inclusion on the particle distribution on the substrate surface.

Keywords CFD modeling, curved substrate, in-flight particle behavior, plasma spray

1. Introduction

Plasma spraying, a subset of thermal spraying process, is a technique by which finely divided metallic or nonmetallic (typically ceramic) materials are deposited in a molten or semimolten state on a prepared substrate. It is widely used to produce coatings easily and flexibly with excellent wear and corrosion (Ref 1, 2), thermal (Ref 3), or fracture (Ref 4) resistance. It is a complex process in which various process parameters, such as power source, nozzle parameter, feeding stock selection, injection methods, substrate conditions, and so forth, contribute synergetically to the final coating quality. This makes the optimization of the plasma spray difficult in experiments and industry (Ref 5, 6). Numerical modeling has become a powerful and effective tool to improve plasma spray processes.

Considerable attention has been paid to research (experiments and simulations) on plasma field parameters and in-flight particle behavior, especially the particle temperatures and velocities, which are the most important parameters affecting the final coating quality (Ref 7-9). Zhang et al. (Ref 6) showed that a small particle injection angle and a high carrier gas flow favored the particle melting and flattening. Westhoff et al. (Ref 10) found that the turbulent dispersion of the particles caused by fluctuating velocity components did not significantly affect the axial velocity distributions of the particles, and the radial velocities in the plume may be very important in determining the particle trajectories. Williamson et al. (Ref 11) did a systematic study to investigate various particle-related phenomena. They found particle size distribution and injection velocity distribution were the most important factors affecting the particle dispersion in the injection direction. However, the aforementioned work was done for cases without consideration of the effect of a substrate obstacle inclusion. So far, not too much attention was devoted to the simulation with substrate inclusion. Martin et al. (Ref 12) found the gas flow rate and the distance from the nozzle to the product surface are the main variables affecting the heat and mass transfer between gas flow and substrates. It is noted in cold spray process, the presence of the substrate and its standoff distance and shape have significant effects on the gas flow field and particle distribution on the substrate, as a result of the influence of bow shock (Ref 13, 14). Kang et al. (Ref 15) found that in plasma spray processing, a flat substrate obstruction at a fixed standoff distance has no effect on the particle distribution.

In industry, especially aerospace and motor industry, a considerable number of mechanical parts are not of a simple flat shape, a case in point being the gas turbine blade. Most of them can be considered a curved shape or composed of some simple shapes including curved

Te Ba and **Heong Wah Ng**, School of Mechanical and Aerospace Engineering, Division of Engineering Mechanics, Nanyang Technological University, 50, Nanyang Ave., Singapore 639798, Singapore; and **Chang Wei Kang**, Institute of High Performance Computing, 1, Fusionpolis Way, No. 16-16, Connexis, Singapore 138632, Singapore. Contact e-mail: MHWNG@ntu.edu.sg.

Nomenclature

a	empirical constant (9.81)
A_p	surface area of the particle (m^2)
C	specific heat capacity (J/kg K)
C_μ	empirical constant (0.09)
C_{1s}	empirical constant (1.44)
C_{2s}	empirical constant (1.92)
C_∞	specific heat capacity of the plasma (J/kg K)
C_p	specific heat capacity of yttria-stabilized zirconia (J/kg K)
C_D	drag coefficient
D	diffusion coefficient (m^2/s)
D_p	particle diameter (m)
E	arc voltage (V)
F_D	viscous drag force of the particle (N)
G_K	product of the eddy viscosity and viscous dissipation terms
H	enthalpy (J/kg)
h	heat transfer coefficient (W/m K)
h_{lt}	latent heat of vaporization (J/kg)
I	arc current (A)
I_t	turbulent intensity (%)
m_p	mass of particle (kg)
k_p	thermal conductivity of yttria-stabilized zirconia (J/kg K)
k_∞	thermal conductivity of plasma (J/kg K)
K	von Kármán constant (0.42)
L	length of the curved substrate
p	pressure (Pa)
P_{in}^W	constant heat source (W/m^3)
$\dot{q}$	heat flux (W/m^2)
Q_c	convective heat transfer (J)
$R1$	inner radius of the curved substrate
$R2$	outer radius of the curved substrate
Re_d	Reynolds number based on the particle diameter (m/s)
S_ϕ	source term
T_b	boiling point of yttria-stabilized zirconia (K)
T_m	melting point of yttria-stabilized zirconia (K)
T_E	plasma temperature at an element point adjacent to the wall (K)
T_i	initial particle temperature (K)
T_p	particle temperature (K)
T_w	plasma temperature on the substrate wall (K)
T_∞	local temperature of the plasma (K)
u, v, w	velocity components in x, y, and z directions, respectively (m/s)
U	velocity magnitude (m/s)
U_E	plasma velocity at an element point adjacent to the wall (m/s)
V	volume (m^3)
$\mathbf{V}$	plasma velocity vector (m/s)
$\bar{\mathbf{V}}$	mean velocity vector (m/s)
$\mathbf{V}'$	velocity vector fluctuation (m/s)
V_n	volume fraction for species n
$\mathbf{V_p}$	particle velocity vector (m/s)
W	width of the curved substrate
W_p	energy increase of the particle (J)
X_p	position of the particle motion
y	distance from element to the wall (m)
Y_n	mass fraction for species n
y_E	distance from adjacent element point to the wall (m)

Subscript

∞	far field region
l	laminar state
p	particle
t	turbulent state
mix	mixture properties

Greek symbols

α	thermal diffusivity (m^2/s)
ε	turbulent kinetic energy dissipation rate (m^2/s^2)
η	torch efficiency (%)
Γ_ϕ	diffusion coefficient
κ	turbulent kinetic energy (m^2/s^2)
κ_E	turbulent kinetic energy at adjacent element point to the wall (m^2/s^2)
μ	dynamic viscosity (kg/ms)
ν_p	kinematic viscosity (m^2/s)
ϕ	process variable
ρ	density of plasma (kg/m^3)
ρ_p	density of zirconia (kg/m^3)
τ_W	wall shear stress (Pa)

Dimensionless numbers

Pr	Prandtl number
Re	Reynolds number
U^*	dimensionless mean velocity
y^*	dimensionless distance from element to the wall
y_T^*	dimensionless thermal sublayer thickness

surfaces. So it is very important to investigate the plasma parameters and in-flight particle behaviors under the influence of curved substrates. However, not too much simulation research has been conducted for curved substrate inclusion until now.

The purpose of this article is to present a numerical three-dimensional (3D) model constructed to investigate the plasma field and in-flight particle behavior with or without inclusion of curved substrates. The three-dimensional computing domain encompasses the torch inlet and injection port, and the air region in front of the torch, including the solid substrate obstruction. A constant volumetric heat source is used to model the plasma generation, while the one-way coupling scheme is used to

solve the plasma-particle interaction. Various lines and surfaces are used to acquire the data, followed by presenting and discussing individual and combined results that are obtained.

2. Modeling and Simulation Methodology

2.1 Geometry Design

A schematic illustration of the plasma torch gun of SG-100 (Praxair Surface Technologies Inc., Appleton, WI) is shown in Fig. 1. The area delineated by the thick solid lines is defined as *upstream computational domain*; adjacent to it, a virtual *downstream computational domain* is created, encompassed by the nozzle front face and thick dashed lines. The downstream computational domain is in a cylindrical shape with the dimensions of ∅160 mm (diameter) by 250 mm (length). It is necessary to mention that for a clear illustration purpose, the downstream computational domain is not proportional to the upstream computational domain in Fig. 1. The entire computational domain is presented in Fig. 2.

The geometrical shape of the curved substrates is illustrated in Fig. 3, with dimensions of width W, length L, inner radius $R1$, and outer radius $R2$. The axes of curvature are positioned orthogonally with respect to the carrier gas injection direction (shown as dashed line), as shown in Fig. 4—the model with concave surface of the substrate facing to the torch exit is labeled as "C"; when the convex surface is facing the torch exit, it is labeled as "V". In addition, as shown in Fig. 1, these substrates are positioned in front of the nozzle front face with a distance of 80 mm between this face and the substrate front face center. The torch axis passes through the substrate front face center in the normal direction of the substrate front face.

Together with the case without substrate inclusion, five cases are conducted to assess the effect of shape and orientation on plasma field temperature and velocity: Free-stream (Fr), two concave, and two convex cases as in Table 1. All the substrates have the same length (L) 50 mm; other specifications in these cases are also listed in Table 1.

2.2 Computing Strategy

Integration of structured and unstructured schemes is used to generate elements throughout the entire geometry by using Gambit V2.3.16; the model is further solved by

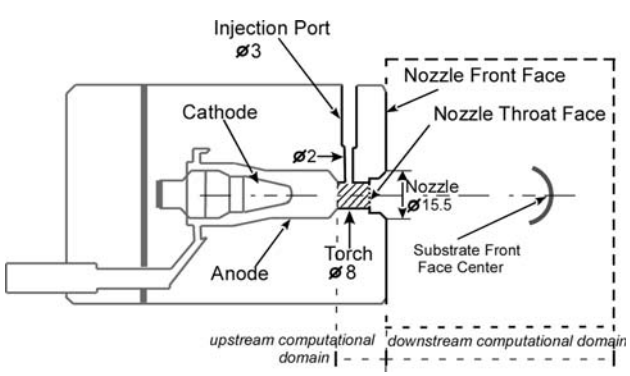

Fig. 1 SG-100 torch gun

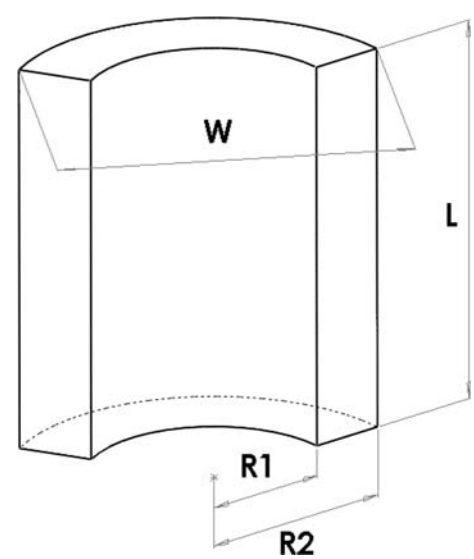

Fig. 3 Substrate shape

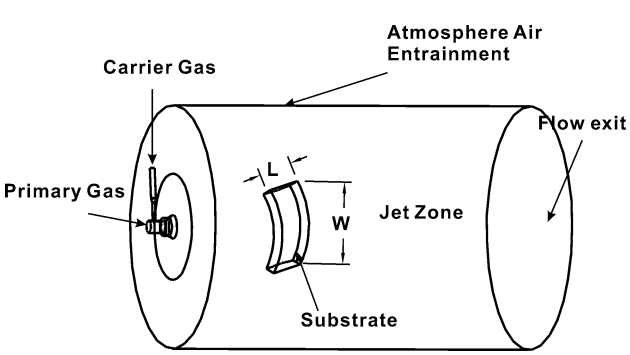

Fig. 2 Model of computational domain of plasma spray

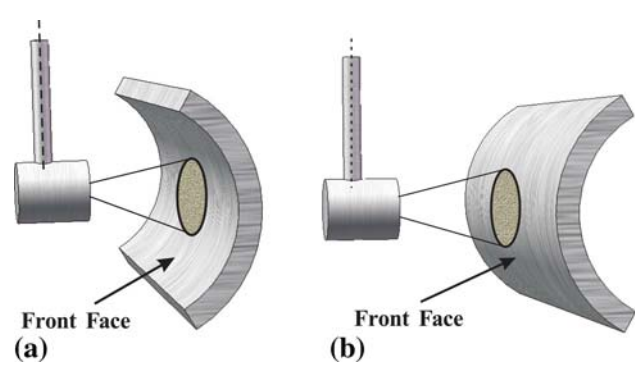

Fig. 4 Substrate orientation. (a) Concave case. (b) Convex case

Table 1 Dimensional specifications and orientations of substrates in five model cases

Case	*L*, mm	*W*, mm	*R*1, mm	*R*2, mm
Fr	...	...	...	...
S1-C	50	25	11	13
S1-V	50	25	11	13
S2-C	50	55	51	57
S2-V	50	55	51	57

Fluent V6.3.26. The adopted total number of grids is around 70,000 cells for the Freestream case. The number increases with the inclusion of the substrate.

Moreover, several assumptions are adopted to establish this model.

- The torch is equipped with a straight gas injector; therefore, primary gas is injected normally from gas injector into the torch, and no swirl is present in the plasma heat generation.
- The plasma is considered as optically thin, that is, transparent to radiative heat transfer.
- As the lateral boundary of the external domain is a distance far away from the exit of the nozzle, an atmospheric boundary is imposed there.
- Because of the high velocity of the plasma flow, the inertia is the dominant force compared with the buoyancy force or the gravity effect. Therefore, no other sources than the inertia is included.
- The plasma fluid flow is assumed as incompressible and in a steady state.
- The plasma gas is chemically inert, with temperature-dependent thermodynamic and transport properties in local thermodynamics equilibrium (LTE) assumption. Properties of argon and air are adopted from literature (Ref 16) and fitted into a piecewise linear profile in FLUENT.
- Because of the small sizes and high velocity of the in-flight particles, gravitational force is negligible compared with the viscous drag force.
- Because of the high temperature of the plasma field (about 12,000 K) and small size of the feedstock particles, the particles are assumed to be liquid droplets once they enter the plasma field.

2.3 Plasma Flow Modeling

2.3.1 Governing Equations. The general governing equation for plasma flow can be written as a differential form as:

$$\nabla \cdot (\rho \mathbf{V} \phi) = \nabla \cdot \left(\Gamma_\phi \nabla \phi\right) + S_\phi \qquad \text{(Eq 1)}$$

where ϕ is the process variable and $\mathbf{V}$ the velocity vector. Process variables ϕ, diffusion coefficients Γ_ϕ, and the source terms S_ϕ represent different combinations of variables in different conservation equations, which are shown in Table 2.

Table 2 Process variables, diffusion coefficients, and source terms for Eq 1

Equation	Variable (ϕ)	Diffusion coefficient (Γ_ϕ)	Source term (S_ϕ)
Mass	l	0	0
Momentum	u, v, w	$\mu_l + \mu_t$	$-\nabla p$
Energy	H	$k_l + k_t$	P_{in}^{W}
Species	Y_n	$D_l + D_t$	0
Turbulence	κ, ε	$\mu_l + \frac{\mu_t}{Pr_{t,k}}$, $\mu_l + \frac{\mu_t}{Pr_{t,z}}$	$G_k - \rho\varepsilon$, $C_{1s}\frac{\varepsilon}{k}G_k - C_{2s}\rho\frac{\varepsilon^2}{k}$

2.3.2 Plasma Heat Generation. Argon gas is used as a primary and carrier gas. A volumetric heat source defined by source term P_{in}^{W} is included in the governing energy equation to approximately represent the arc heating:

$$P_{in}^{W} = \frac{\eta E I}{V} \qquad \text{(Eq 2)}$$

where P_{in}^{W} is the volume-averaged heat source, E is the arc voltage, I is the arc current, and V is the volume of the anode, which is shaded with diagonal line patterns in Fig. 1. Torch efficiency, η is set as 67% (Ref 17), which takes heat loss caused by cooling water into account.

2.3.3 Gas Mixing. When the plasma gas is released into the atmosphere, entrainment and mixing of atmospheric air into the plasma jet (argon) occur. To calculate the mixture properties of these two species, mixing laws are adopted. Volume-weighted mixing law is applied for mixture density while mass-weighted mixing law is adopted for the other properties.

Mixture Density:

$$\rho_{mix} = \frac{\sum_n V_n \rho_n}{\sum_n V_n} = \frac{\sum_n (Y_n/\rho_n)\rho_n}{\sum_n (Y_n/\rho_n)} = \frac{1}{\sum_n (Y_n/\rho_n)} \qquad \text{(Eq 3)}$$

Mixture Specific Heat:

$$C_{mix} = \frac{\sum_n Y_n C_n}{\sum_n Y_n} = \sum_n Y_n C_n \qquad \text{(Eq 4)}$$

Mixture Thermal Conductivity:

$$k_{mix} = \frac{\sum_n Y_n k_n}{\sum_n Y_n} = \sum_n Y_n k_n \qquad \text{(Eq 5)}$$

Mixture Viscosity:

$$\mu_{mix} = \frac{\sum_n Y_n \mu_n}{\sum_n Y_n} = \sum_n Y_n \mu_n \qquad \text{(Eq 6)}$$

where V_n is the volume fraction and Y_n the mass fraction for species n.

2.3.4 Wall Functions. The flow behavior and turbulence structure of turbulent flow may be significantly affected by the inclusion of the solid substrate, especially the position and shape of substrate. Velocity decreases sharply in the near-wall region. Large velocity gradients result in a high turbulence area around the substrate. In order to bring the simulation closer to reality, a series of semiempirical formulas are used to associate the viscosity-affected region with the wall and the fully turbulent region.

Based on Launder and Spalding's proposal (Ref 18), U_E, τ_W, T_E, T_W, $\dot{q}$, and y are defined, respectively, as the time-average plasma velocity at adjacent element E along the wall, the shear stress along the velocity direction, the time-average temperatures at points E and W, the heat flux to the wall, and the distance from the wall. E represents an element point adjacent to the wall, while W is the projection point of E on the wall. The following equation, which is called the "law-of-the-wall" for mean velocity, is used as the wall functions (Ref 19).

$$U^* = \begin{cases} \frac{1}{K}\ln(ay^*), & y^* \geq 11.225 \\ y^*, & y^* < 11.225 \end{cases} \quad \text{(Eq 7)}$$

where U^*, the dimensionless velocity, and y^* the distance from the element to the wall are defined as:

$$U^* = \frac{U_E C_\mu^{1/4} \kappa_E{}^{1/2}}{\tau_W \rho} \quad \text{(Eq 8)}$$

$$y^* = \frac{\rho C_\mu^{1/4} \kappa_E{}^{1/2} y_E}{\mu} \quad \text{(Eq 9)}$$

C_μ has an empirical constant value 0.09, κ_E is the turbulence kinetic energy at point E, while y_E is the distance from point E to the wall.

The logarithmic law for mean temperature is similar to that for mean velocity, according to Reynolds analogy between momentum and energy transport. The law-of-the-wall for temperature employed in FLUENT is shown as:

$$T^* \equiv \frac{(T_W - T_E)\rho C_\infty C_\mu^{1/4} \kappa_E^{1/2}}{\dot{q}} = \begin{cases} \Pr y^*, & y^* < y_T^* \\ Pr_t\left[\frac{1}{K}\ln(ay^*) + P\right], & y^* \geq y_T^* \end{cases} \quad \text{(Eq 10)}$$

where C_∞ is the plasma specific heat capacity, $\dot{q}$ the flux heat to the substrate, y_T^* the nondimensional thermal sublayer thickness. The value of P is given by (Ref 20):

$$P = 9.24\left[\left(\frac{Pr}{Pr_t}\right)^{3/4} - 1\right]\left(1 + 0.28e^{-0.007Pr/Pr_t}\right) \quad \text{(Eq 11)}$$

where Pr is the Prandtl number, $Pr = \mu/\alpha$, a function of temperature. When $y^* < y_T^*$, the equation is the linear law for the thermal conduction sublayer where conduction is important; while when $y^* > y_T^*$, it becomes the logarithmic law for the turbulent region where effects of turbulence dominate conduction (Ref 19).

2.4 Operating Parameters and Boundary Condition

The operating parameters are listed in Table 3, including the torch specifications briefly annotated in Fig. 1. Inlets of the torch and injector are both modeled as a mass flow inlet to achieve a better convergence rate compared with that of a pressure inlet. The mass flow rates of primary gas and carrier gas are assigned, respectively, to torch and injector port. All the torch gun walls are set at a constant temperature of 300 K, which is the ambient temperature. Boundaries of downstream computational domain are set as pressure outlet, where atmospheric condition is imposed. Turbulence model at inlets of the torch and injectors are characterized by turbulent intensity and hydraulic diameter. The turbulent intensities at arc gas and carrier gas inlets can be calculated by:

$$I_t = 0.16Re^{-1/8} \quad \text{(Eq 12)}$$

where Re is the Reynolds number of respective inlets, on the basis of hydraulic diameter and characteristic length.

Table 3 Operating parameters for plasma simulation

Operating parameters	Units	Magnitudes
Torch diameter	mm	8
Nozzle diameter	mm	15.5
Injection port diameter	mm	3
Substrate standoff distance	mm	80
Powder size	μm	22-125
Current input	A	900
Voltage	V	35
Torch efficiency	%	67
Heat source	W/m^3	4.4178×10^{10}
Arc gas (argon) flow rate	kg/s	1.9474×10^{-3}
Carrier gas (argon) flow rate	kg/s	1.136×10^{-4}
Turbulence intensity at arc gas inlet	%	4.83
Turbulence intensity at carrier gas inlet	%	6.09

Table 4 Thermodynamic and physical properties of yttria-stabilized zirconia

Property	Denotation	Units	Magnitudes
Density	ρ_p	kg/m^3	5890
Melting point	T_m	K	2988
Boiling point	T_b	K	5273
Kinematic viscosity	ν_p	m^2/s	6.5×10^{-6}
Thermal conductivity	k_p	W/m K	2.4
Latent heat of vaporization	h_{lt}	J/kg	6×10^6
Specific heat capacity	C_p	J/kg K	(a)

(a) $C_p = 1.06343 \times 10^{-6}\ T_p^3 - 2.188953 \times 10^{-3}\ T_p^2 + 1.709671\ T_p + 1.466367 \times 10^2$, 273 K $< T_p <$ 873 K; $C_p = 678.5$, $T_p >$ 873

2.5 Particle Dynamics and Heat Transfer Modeling

The thermodynamic and transport properties of zirconia required in the simulation are shown in Table 4. On the basis of the obtained converged plasma field, zirconia particles are injected axially through an internal injection port. The flow of particles is modeled by FLUENT, using the discrete phase model in a Lagrangian frame of reference. A fundamental assumption made in this model is that the dispersed second phase occupies a low volume fraction, which means the second phase is sufficiently dilute that particle-particle interactions and the effects of the particle volume fraction on the gas phase are

negligible. Motion of a particle is defined as a function of its velocity:

$$\frac{dX_p}{dt} = \mathbf{V_p} \quad \text{(Eq 13)}$$

where the particle velocity $\mathbf{V_p}$ can be determined from a momentum balance for the particle by

$$m_p \frac{d\mathbf{V_p}}{dt} = F_D \quad \text{(Eq 14)}$$

where m_p is the mass of single particle, while F_D, the viscous drag force, is defined as:

$$\mathbf{F_D} = \frac{18\mu}{\rho_p D_p^2} \frac{C_D Re}{24(\mathbf{V} - \mathbf{V_p})} \quad \text{(Eq 15)}$$

where Re is the local relative Reynolds number with the following definition:

$$Re = \frac{\rho D_p |\mathbf{V} - \mathbf{V_p}|}{\mu} \quad \text{(Eq 16)}$$

while the drag coefficient C_D, typically is given as a function of Reynolds number:

$$C_D = a_1 + \frac{a_2}{Re} + \frac{a_3}{Re^2} \quad \text{(Eq 17)}$$

where a_1, a_2, and a_3 are constant coefficients over several ranges of Reynolds number (Ref 21), which are listed in Table 5.

For comparison purposes, turbulence flow effect on the particle trajectories is ignored for the inaugural cases of the in-flight particle simulation. In such a case, the trajectory is computed based on the mean continuous phase velocity field (Eq 14). After that, a stochastic tracking method, *Random Walk Model*, is used to predict the dispersion of particles caused by turbulence. In this approach, the instantaneous value of the fluctuating gas flow velocity is included:

$$\mathbf{V} = \bar{\mathbf{V}} + \mathbf{V}' \quad \text{(Eq 18)}$$

where $\bar{\mathbf{V}}$ is the mean velocity vector, and $\mathbf{V}'$ is the velocity vector fluctuation. The trajectory equations are integrated along the particle path by using the instantaneous flow velocity. By computing the trajectory in this manner for a sufficient number of representative particles, the random effects of turbulence on the particle turbulence may be accounted for. In the plasma spray process, the radiative heat losses from the particle are negligible compared with the convective heat flux from the plasma to the particle (Ref 22). Therefore,

$$m_p C_p \frac{dT_p}{dt} = hA_p(T_\infty - T_p) + \frac{dm_p}{dt} h_{lt} \quad \text{(Eq 19)}$$

where m_p is the mass of the particle, C_p is the specific heat capacity of the particle, T_p is the local temperature of the continuous phase, A_p is the surface area of the particle, and h_{lt} is the latent heat of vaporization. The heat transfer coefficient, h is defined using the correlation of Ranz and Marshall (Ref 23):

$$h = k_\infty / D_p \left(2.0 + 0.6[(Re)]_d^{(1/2)} \left[(Pr)^{(1/3)}\right]\right) \quad \text{(Eq 20)}$$

where k_∞ is the thermal conductivity of the plasma phase, Re_d means the Reynolds number based on the particle diameter and the relative velocity, and Pr is Prandtl number of the continuous phase. The first term on the right hand of Eq 19 is the convective heat transfer; while the second one is the latent heat transfer through evaporation and condensation. When the particle temperature is below the particle melting point, the second term can be omitted, which means the process is considered an inert heating or cooling process.

Table 5 Value of constant coefficients a_1, a_2, and a_3 over different Reynolds number ranges

Reynolds Number	a_1	a_2	a_3
$Re < 0.1$	24.0	0	0
$0.1 < Re < 1.0$	22.73	0.0903	3.69
$1.0 < Re < 10$	29.1667	−3.8889	1.222
$10.0 < Re < 100.0$	46.5	−116.67	0.6167
$100.0 < Re < 1{,}000.0$	98.33	−2778	0.3644
$1{,}000.0 < Re < 5{,}000.0$	148.62	-4.75×10^4	0.357
$5{,}000.0 < Re < 10{,}000.0$	−490.546	5.787×10^5	0.46
$10{,}000.0 < Re < 50{,}000.0$	−1,662.5	5.4167×10^6	0.5191

3. Results and Discussion

3.1 Data Acquisition Lines and Surfaces

In order to analyze the simulation result, data of interest are extracted along several surfaces (or lines). As shown in Fig. 5, the line PQ along z-axis is referred as *Centerline*; two plane-shape longitudinal sections at $x = 0$ and $y = 0$ are referred to as, respectively, *YZ plane* (blue color) and *XZ plane* (green color).

Moreover, two parallel surfaces of the substrate front face, named "parallel data acquisition surface," are created to get the near-substrate-wall flow field behavior. Figure 6 illustrates the side view of such a parallel data acquisition surface, which has a distance D_w to the substrate front face. These two parallel surfaces are referred to as, respectively, *Near Surface* with $D_w = 0.1$ mm and

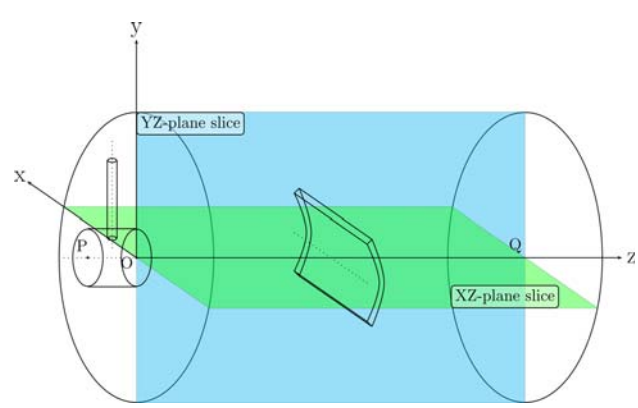

Fig. 5 Centerline and XZ and YZ planes

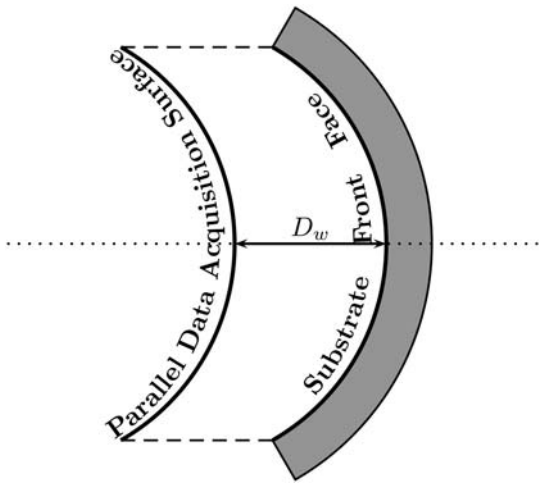

Fig. 6 Side view of parallel data acquisition surface

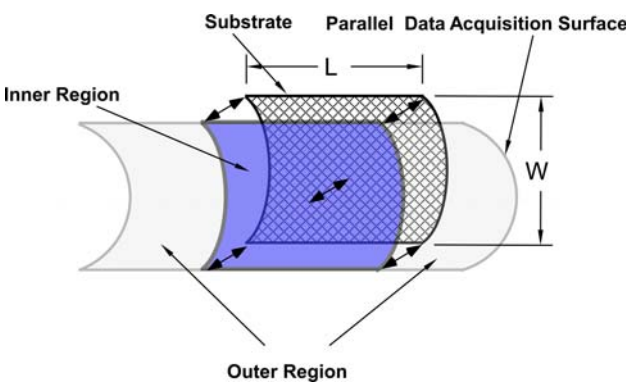

Fig. 7 Inner Region and Outer Region of the "parallel data acquisition surface"

Far Surface with $D_w = 5$ mm. It is necessary to mention that the length of the "parallel data acquisition surfaces" extends in both directions within the downstream computational domain, while the substrate front face is of a length L, as shown in Fig. 7. The cross-hatched surface represents the substrate front face, while the surface in front of it is the "parallel data acquisition surface." The region on the "parallel data acquisition surface" directly ahead of the substrate front face, is referred to as *Inner Region*; while the extended regions at sides of the Inner Region are referred to as *Outer Region.*

For visualization convenience, a flattening procedure maps specific curvilinear coordinates of the "parallel data acquisition surface" (Near or Far) (Fig. 8a) into a planar representation without distortion (Fig. 8b). The resultant surface is called *Developed Surface*, with a transformed Y coordinate $Y' = R\theta$.

3.2 Grid Independence Test and Verification of Simulation Model

A grid independence test is conducted on the mesh models at the beginning of the simulation work to ensure

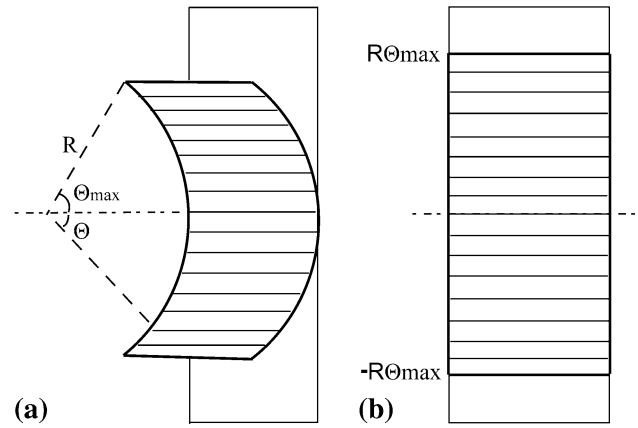

Fig. 8 Flattening parallel curved surface into Developed Surface. (a) Original surface. (b) Developed Surface

an optimized mesh scheme was obtained. It is carried out for Freestream case with three levels of grid size: coarse with total number of grids as 715,161, medium 1,475,949, and fine 2,174,076. These three levels are roughly in a ratio of 1×, 2×, and 3× the number of grids of the coarse model, respectively. The plasma temperature and velocity magnitude are extracted from XZ plane to monitor the effects of the mesh refinement, which are shown in Fig. 9. The coarse, medium, and fine model are illustrated, respectively, by solid, dashed, and dotted lines. There is not much discrepancy between these three levels, and an average of about 3% difference is found between adjacent levels. Therefore, the coarse grid scheme is adopted for the following work because the consumption of computing time and resource is less.

In order to verify the current simulation model, another model is constructed according to the experimental setup by McKelliget et al. (Ref 24). This model is simulated based on the operating conditions of 7.4 kW power input and 35.4 L/min of argon gas flow rate. The mathematical laws, the assumptions, and boundary conditions setting remain as the current simulation model discussed previously. Meanwhile, a comparison model is set up with turbulence correction advised by Bolot et al. (Ref 25).

Figure 10(a) and (b) shows, respectively, the plasma temperature and axial velocity distribution along the Centerline. The square scatters, solid lines, and dashed lines are the experimental data from McKelliget et al. (Ref 24), result of the model without turbulence correction and the model with turbulence correction, respectively. Both models (with and without turbulence correction) can predict the plasma temperature and velocity reasonably well. It can be seen that plasma jet core of the current model is shorter than the turbulence correction model, but closer to the experimental data at a relatively far distance away from the torch exit. Because the intention of our current work is to investigate the influence of curved substrates on the plasma field, especially the particle behavior far away from the plasma jet core; therefore, the current model without turbulence correction is adopted.

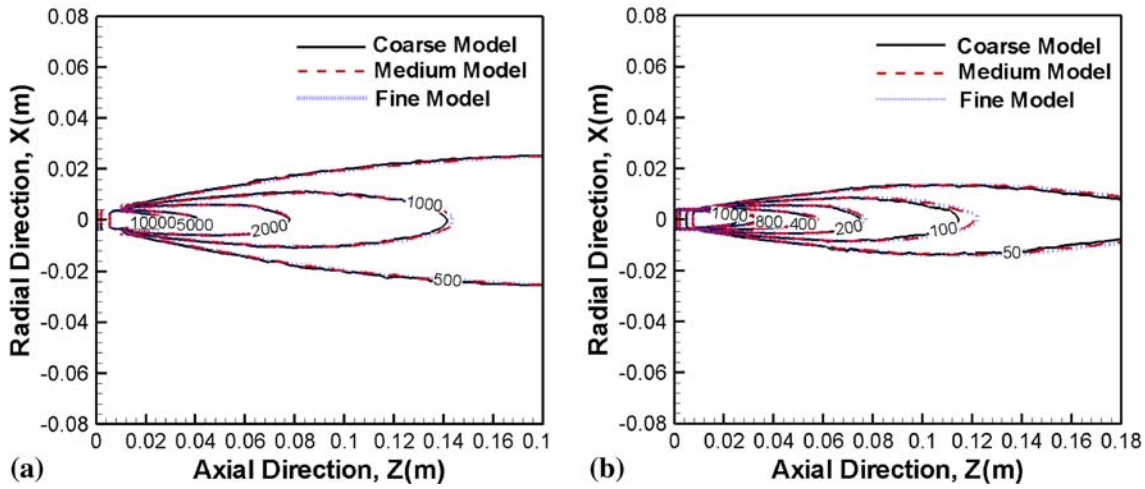

Fig. 9 Grid independence tests for Freestream by comparison of contours of (a) temperature and (b) velocity in *XZ* plane

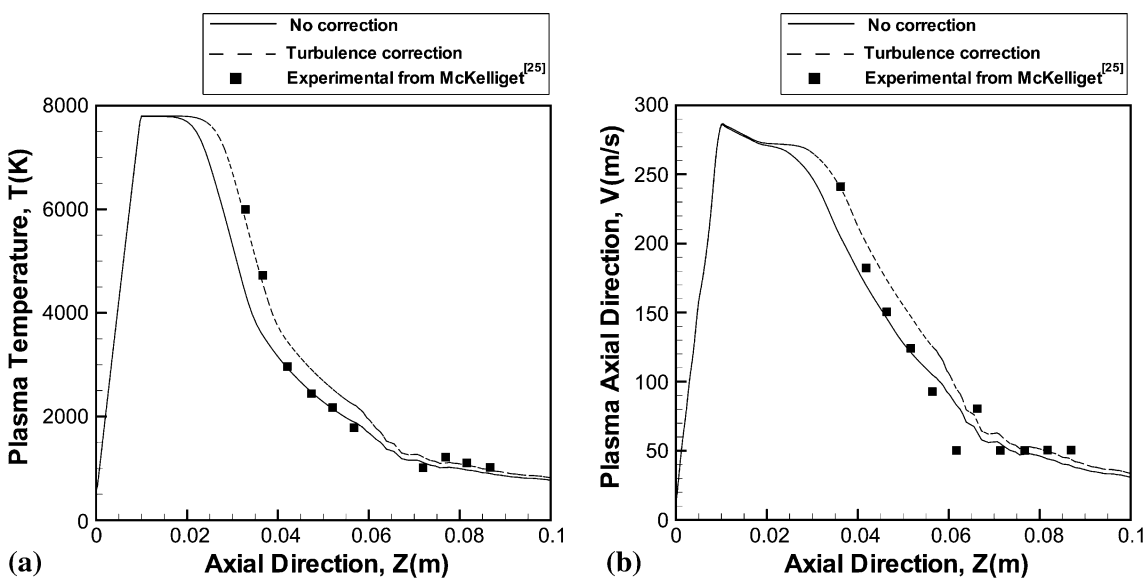

Fig. 10 Verification of simulation model by comparison with experimental data from McKelliget et al. (Ref 24) in (a) temperature and (b) axial velocity along Centerline

3.3 Temperature and Velocity Distribution Along Axial Centerline

Figure 11(a) shows the plasma temperature distribution along the centerline for the five cases. Because of the high intensity arc, the plasma temperature increases sharply at the upstream of nozzle throat face; the expansion effect of argon gas caused by high temperature results in a similar plasma velocity profile (Fig. 11b).

Temperature and velocity start to drop immediately after the nozzle throat face, at a relatively small reduction rate. The temperature (also the velocity) decreases drastically to ambient condition approximately 20 mm downstream of the nozzle front face. Plasma velocities of those cases with inclusion of substrates initially almost coincide with the Freestream case up to nearly 20 mm upstream of the substrate front face, where they start deviating from the Freestream cases because of the obstruction effect. Compared with plasma velocity, the obstruction effect on the plasma temperature is relatively minor, until approximately 10 mm upstream. The temperature drop across the substrates is more drastic than that occurring upstream of the substrate front face. For different cases, the temperature drop intensity is nearly the same, but at different temperature decreasing rates, which varies inversely as the substrate thickness. This phenomenon is shown clearly in Fig. 11(a).

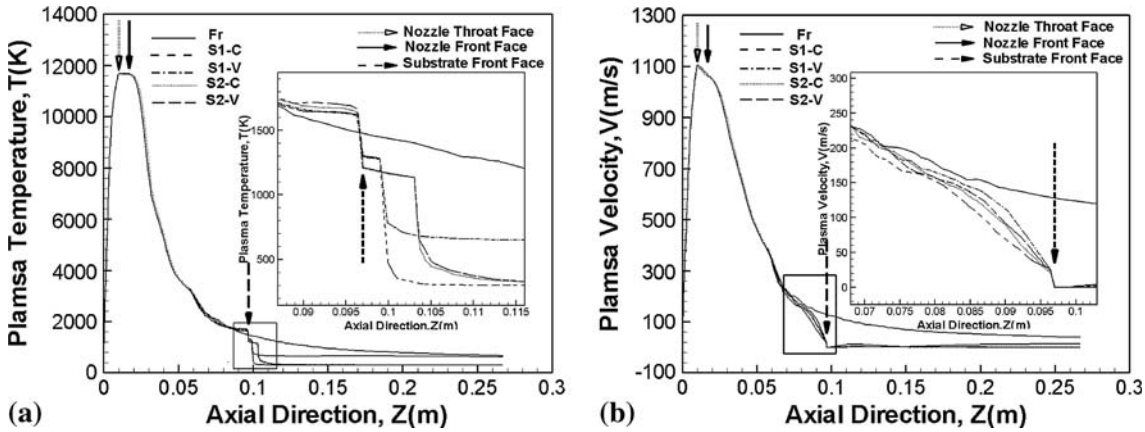

Fig. 11 Prediction of axial Centerline distribution of (a) plasma temperature and (b) plasma velocity

3.4 Thermal Field

Figure 12 presents plasma temperature contours in longitudinal *XZ* and *YZ* planes for the four cases with substrates. The contours are symmetrical about the *YZ* plane (as seen in *XZ* plane view), but not about the *XZ* plane (as seen in *YZ* plane view). There is a deviation of the plasma plume to the negative *Y* direction caused by the carrier gas injection. Temperature curve of the plasma core region with a relatively higher value remains nearly the same shape, as a result of the far distance from the substrates. There is an immediate divergence phenomenon near the substrates: isothermal temperature contour lines follow the substrate shape to some extent. The concave substrate causes a more drastic divergence. When the width of the concave substrate exceeds a certain value, the plasma flow reverses, while there will be a vortex flow when the width of the convex substrate falls below a certain value.

Temperature contours in "parallel data acquisition surfaces" Near Surface and Far Surface are shown in Fig. 13. It seems more regular in Far Surface than that in Near Surface. It is noticed that there is a high-temperature gradient across the shared borders of Inner Region and Outer Regions (at nearly 25 mm along the *X* direction) in Near Surface.

3.5 Velocity Field

As the velocity magnitude contours in *XZ* and *YZ* plane are quite similar to the temperature contours, so only the velocity contour of S1-C case is shown here, in Fig. 14. Figure 15 shows velocity contours in "paralleled data acquisition surfaces" Near Surface and Far Surface. In contrast to the plasma temperature, velocity is more affected by substrate obstruction. There is still a relatively high gradient across the shared borders of the Inner Region and Outer Regions in the Near Surface. Contour shape and velocity magnitude at the Inner Region of Near Surface are totally different from those at its counterpart area in the Far Surface, caused by the stagnation effect. The contour shapes remains similar, and velocity magnitude is changed little in the Outer Region of these two surfaces. The contours are symmetrical with respect to "$X=0$," but deviate to the negative *Y* direction with respect to "$Y'=0$."

Figure 16 shows clearly the plasma velocity streamlines in longitudinal *XZ* and *YZ* planes. Near Surface is used to represent near-substrate-wall region, velocity vectors of which are shown in Fig. 17; velocity magnitude is indicated by arrow length. Initially, the plasma flow develops freely after it exits from the nozzle; but at the near-wall region, the stream is drastically diverted as a result of the substrate obstruction and follows the substrate wall shape. The maximal velocity magnitude is observed at the shared borders of Inner Region and Outer Regions (25 mm in *X* direction). Substrates with smaller curvature (S2) provide an "easier" way for the flow stream to develop, while those with relatively greater curvature (S1) will result in all upward-reversing flow (in *Y* direction) along the substrate front surface for concave case (Fig. 17a) or intensive turbulence at rear area of the substrate (Fig. 16d) for the convex case, which is called "wave" phenomena. The velocity vectors that flow toward the substrate side edges from the circumjacent domain are also caused by such a turbulence effect, as shown in Fig. 17(b).

3.6 Particle In-flight Behavior

In order to have a comprehensive understanding of in-flight particle behavior, two different types of injections are used to set the initial particle injection position for the simulation, illustrated in Fig. 18.

In type (a), referred as "Point Injection", particles are injected at the center of the injection port of the plasma torch; in type (b), referred as "Surface Injection", particles are injected as a group from each cell of the mesh of the injection port. Combined with different particle size ranges, different injection methods are implemented to investigate the in-flight particle features.

In order to investigate the particle size effect on the trajectory, a group of particles with discrete sizes of 22, 47.8, 73.5, 99.5, and 125 μm are injected by "Point

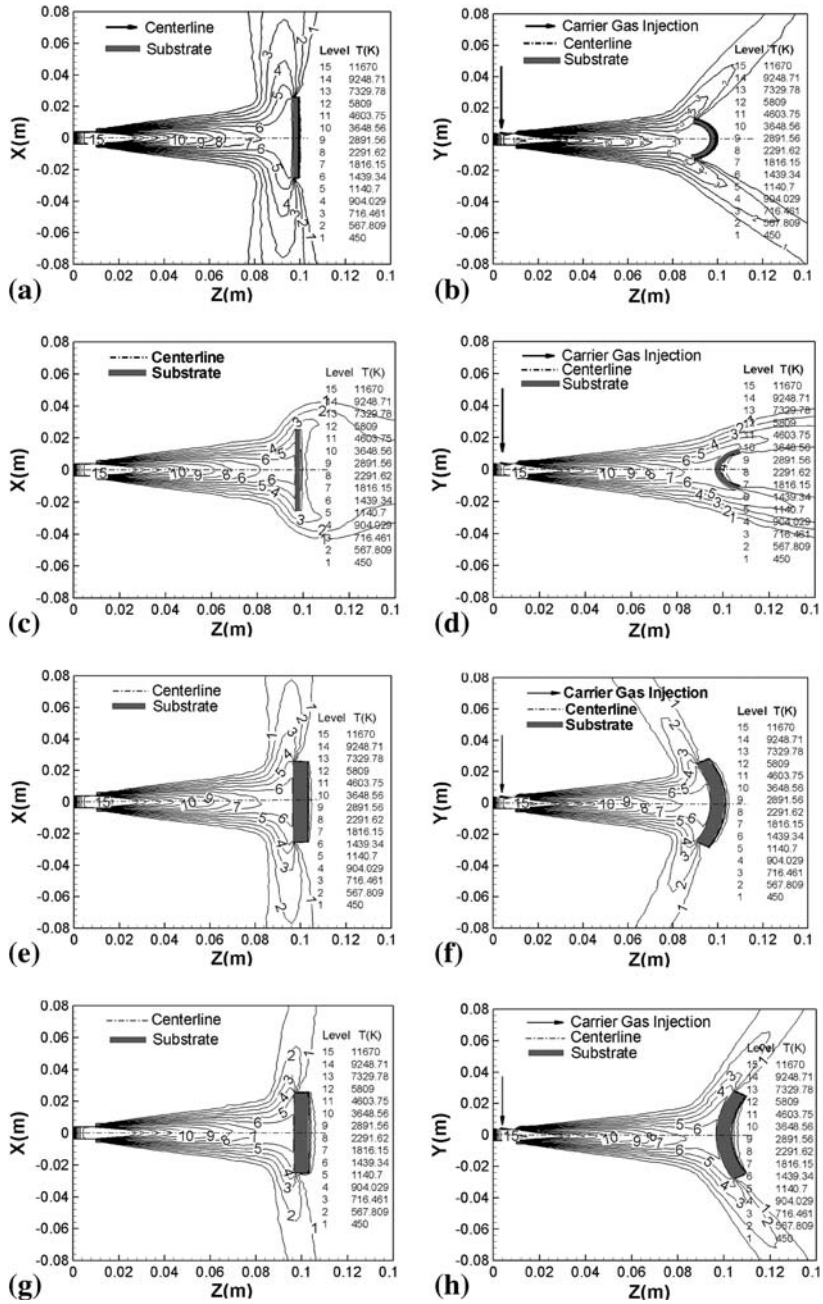

Fig. 12 Comparison of plasma temperature contours in *XZ* and *YZ* planes for four different cases with substrates. (a) *XZ* plane of S1-C case. (b) *YZ* plane of S1-C case. (c) *XZ* plane of S1-V case. (d) *YZ* plane of S1-V case. (e) *XZ* plane of S2-C case. (f) *YZ* plane of S2-C case. (g) *XZ* plane of S2-V case. (h) *YZ* plane of S2-V case

Injection'' in the Freestream case. Figure 19 shows trajectories of these particles within the computing domain; an insert shows part of the trajectories magnified to illustrate the profiles more clearly.

Entrained by the same carrier gas, larger particles are imparted with higher inertia compared with those with smaller sizes, which enables them to penetrate farther across the plasma jet. It can be noted that larger particles tend to have lower trajectories.

At the same time, particle temperatures and velocity profiles along their trajectories are shown, respectively, in Fig. 20 and 21. Both the velocity and temperature of these particles increase drastically when they exit the injector and immediately are entrained by the plasma jet, and after reaching a peak value, start to decrease. Smaller particles have a steeper velocity/temperature gradient and a larger peak value, which is the result of their lower inertia and heat capacity.

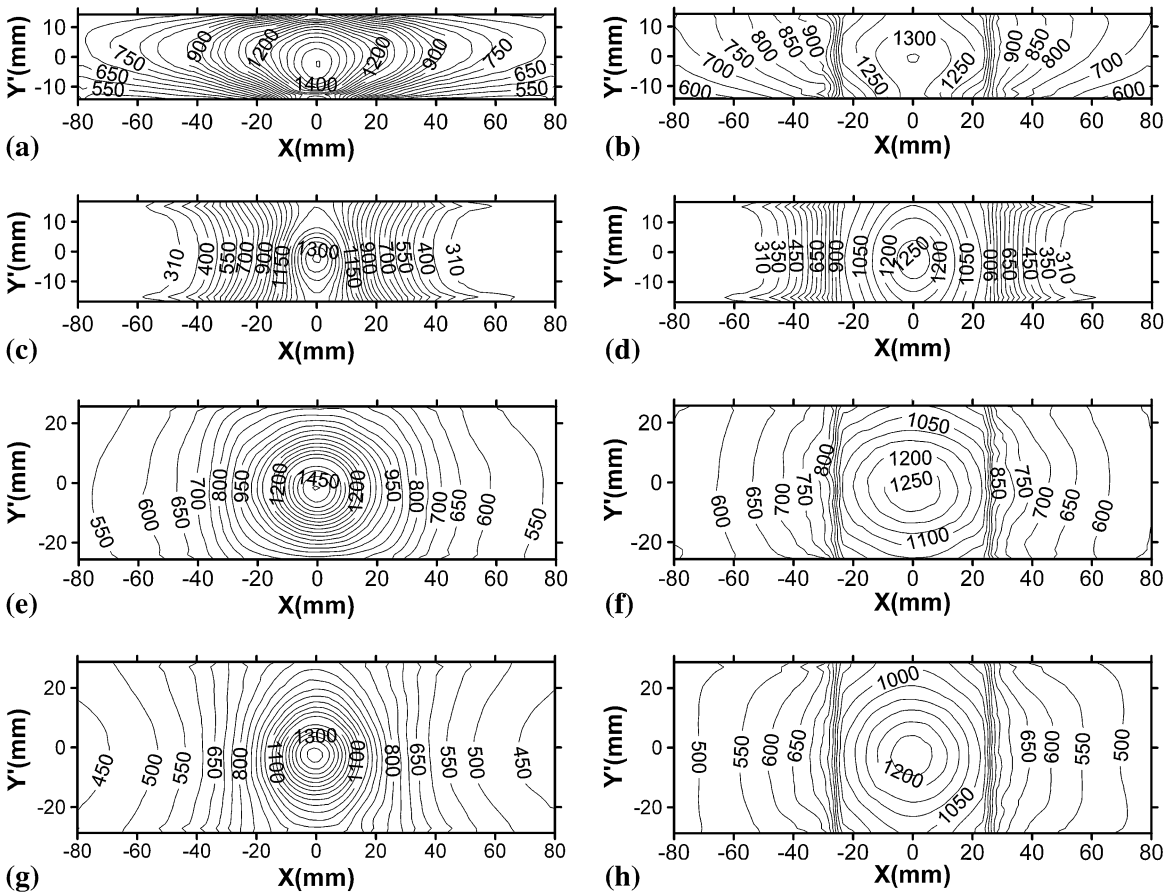

Fig. 13 Temperature contours in Near and Far Surfaces for four different cases with substrates. (a) Far Surface of S1-C case. (b) Near Surface of S1-C case. (c) Far Surface of S1-V case. (d) Near Surface of S1-V case. (e) Far Surface of S2-C case. (f) Near Surface of S2-C case. (g) Far Surface of S2-V case. (h) Near Surface of S2-V case

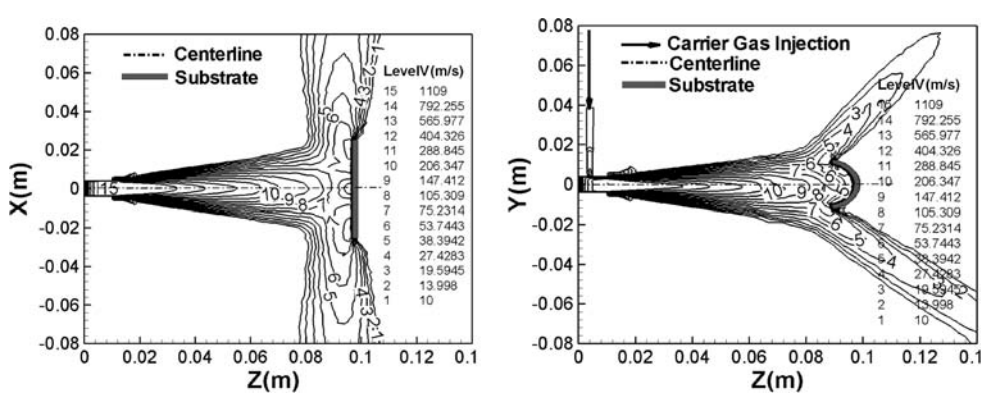

Fig. 14 Comparison of plasma velocity contours in (a) *XZ* and (b) *YZ* plane for S1-C case

In successive works, the S2-C case with particle loading is compared with Freestream case to investigate whether the inclusion of substrate will have an effect on the particle trajectories and further affect the particle distributions on the substrates. For the sake of investigating the effect of plasma flow on small particles with diameter down to several μm, the vaporization and evaporization effects are deactivated to prevent their vanishing during the flight.

Particles with uniform diameters of 3, 5, and 10 μm are injected by "Surface Injection", respectively, in the Freestream case and the S2-C case. All the particles are captured by the substrate and then illustrated on the developed surface of the front face of the substrate. For

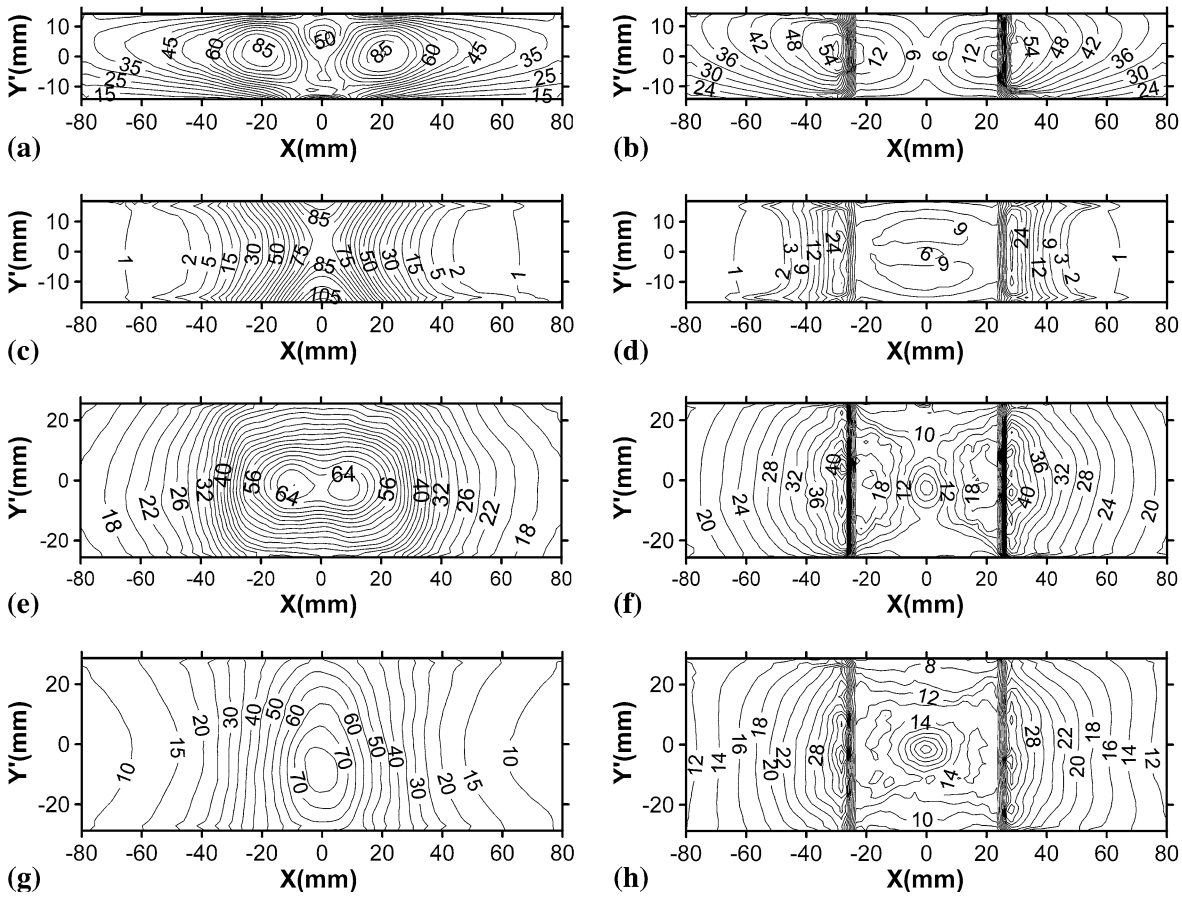

Fig. 15 Plasma velocity contours in Near and Far Surfaces for four different cases with substrates. (a) Far Surface of S1-C case. (b) Near Surface of S1-C case. (c) Far Surface of S1-Vcase. (d) Near Surface of S1-V case. (e) Far Surface of S2-C case. (f) Near Surface of S2-C case. (g) Far Surface of S2-V case. (h) Near Surface of S2-V case

the Freestream case, a virtual substrate with exactly the same geometry as that in S2-case is included to make sure the mesh conditions of these two cases are exactly the same. The virtual substrate is also used for particle capturing. Results are shown in Fig. 22, 23, and 24; it can be seen that smaller particles are more susceptible to the plasma flow deflection by the substrate obstruction. It is obvious that the diverging flow causes the smaller particles to deviate from their freestream trajectories. For 3 μm particles, the upward and sideway flow (refer to Fig. 17c) makes the distribution wider and higher than that in the Freestream case, while for 5 μm particles, the downward flow makes the distribution lower. When the particle diameter increases to 10 μm, the difference becomes insignificant.

From the study above, it can be concluded that there is a threshold of particle diameter, above which the particles are insusceptible to the flow deflection. In the combination of spray parameters (carrier gas flow rate, primary gas flow rate, energy source, injection position and method, etc.) in this work, the threshold is 10 μm.

The dispersion of particles caused by turbulence in the fluid phase is not taken into account in all the above works. In the following work, a stochastic tracking approach is used for particle dispersion prediction. The powder feedstock is defined for a range of diameters between 22 and 125 μm with intervals 1 μm, which is the commercially available powder YSZ particles in experiments. These particles are injected by "Surface Injection" and captured by the substrate. The resultant particle distribution data are postprocessed by a Fortran code and then mapped onto the developed surface of the substrate in a contour form.

Figure 25 shows the contour distributions of particles in terms of diameter, number of particles, temperature, and velocity on the developed surface of the substrate in S2-C case, shown in the left column; while Freestream case is taken for comparison, in the right column. No significant effect of substrate obstruction on the dispersion of particles is observed. This result also confirms the aforementioned conclusion, despite the consideration of particle dispersion. In addition, it is noticed that larger particles tend to accumulate at the lower part of the substrate, with smaller velocity and temperature. However, it is noted that contour of the number of particles have a different contour shape (concentric circles) than those of the other parameters (temperature, velocity, diameter). By superimposing Fig. 25(a) on (e), it is found

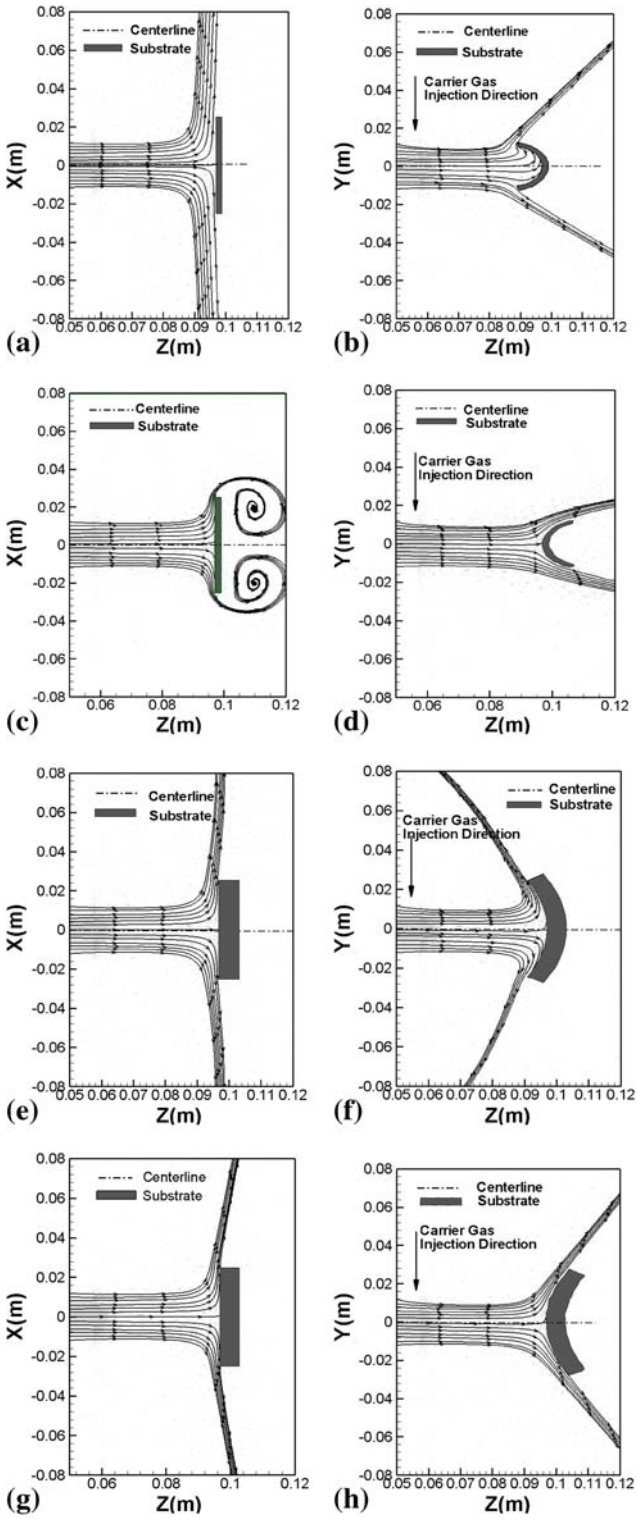

Fig. 16 Plasma velocity vectors in *XZ* and *YZ* planes of four cases with substrates. (a) *XZ* plane of S1-C case. (b) *YZ* plane of S1-C case. (c) *XZ* plane of S1-V case. (d) *YZ* plane of S1-V case. (e) *XZ* plane of S2-C case. (f) *YZ* plane of S2-C case. (g) *XZ* plane of S2-V case. (h) *YZ* plane of S2-V case

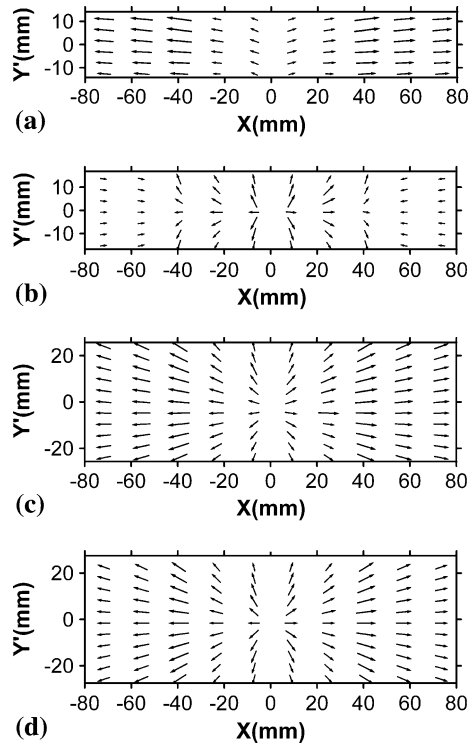

Fig. 17 Plasma velocity vectors in Near Surfaces of four cases with substrates. (a) S1-C case. (b) S1-V case. (c) S2-C case. (d) S2-V case

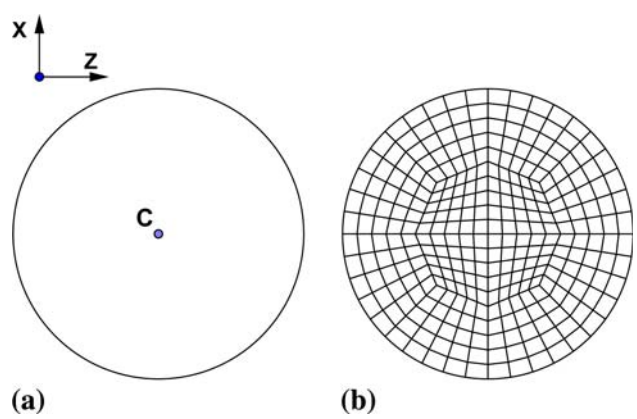

Fig. 18 Injection types. (a) Point injection. (b) Surface injection

that the particles with the medium diameters have the highest concentration.

Figure 26 shows particle mass fraction distribution over different temperature ranges, which is obtained from the particle dispersion data of S2-C. Most of the particles range between the melting point of 2988 K and boiling point of 5273 K for zirconia, implying the majority of particles would have either melted or vaporized, which is

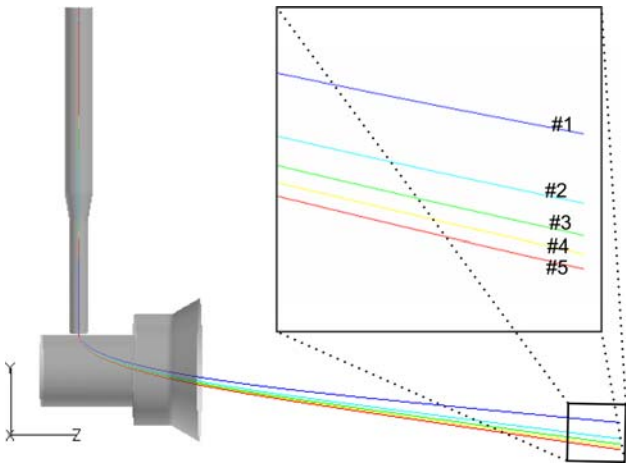

Fig. 19 Trajectories of particles injected from injection port center. No. 1, 22.0 μm; No. 2, 47.8 μm; No. 3, 73.5 μm; No. 4, 99.5 μm; No. 5, 125 μm

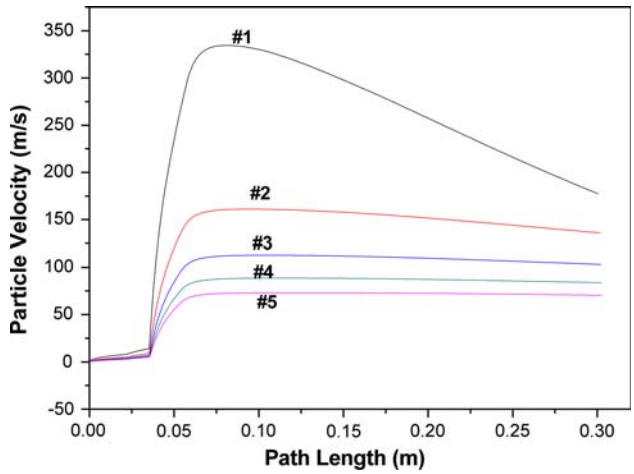

Fig. 21 Particle velocity profile along trajectories. No. 1, 22.0 μm; No. 2, 47.8 μm; No. 3, 73.5 μm; No. 4, 99.5 μm; No. 5, 125 μm

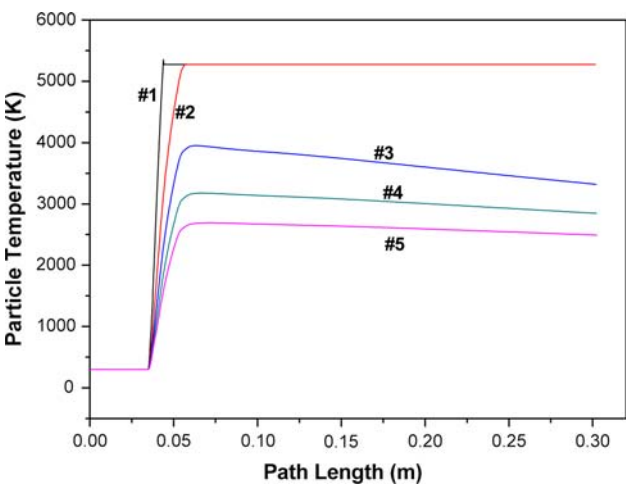

Fig. 20 Particle temperature profile along their trajectories. No. 1, 22.0 μm; No. 2, 47.8 μm; No. 3, 73.5 μm; No. 4, 99.5 μm; No. 5, 125 μm

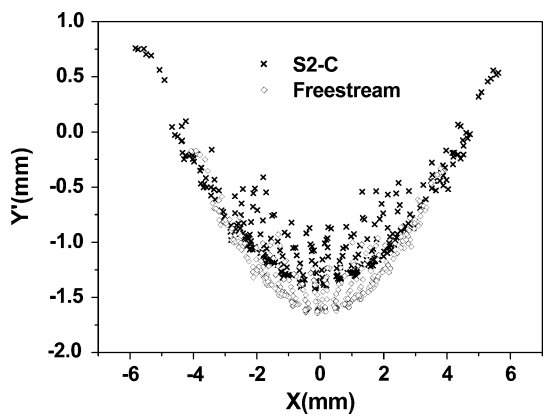

Fig. 22 Particle distribution comparison between Freestream and S2-C with 3 μm uniform particle injection

the expected result for plasma spray coating. It can be seen that a large portion of particles are at the boiling point, which means lots of particles have started to vaporize and the corresponding mass fraction in the figure is the part left after the vaporization. This may be one of the reasons contributing to the relatively low deposition efficiency in plasma spray. Figure 27 shows the particle temperature distribution over different particle sizes. Dark black points form a trend line of mean particle temperatures within the entire particle size range. Smaller particles tend to acquire higher temperature compared with their larger counterparts, which supports the result from Fig. 20 and 25. This phenomenon might be attributed to the relationship between heat transfer and temperature variation. To simplify the explanation, the heat transfer

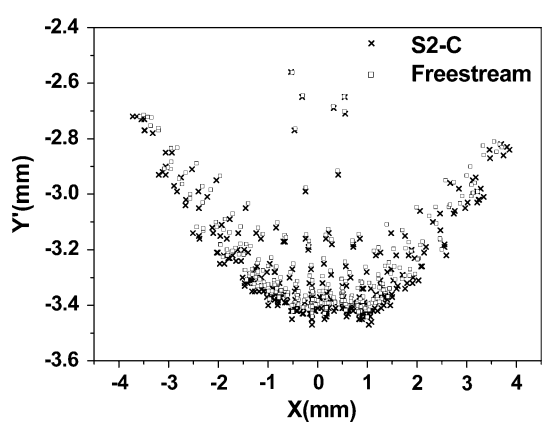

Fig. 23 Particle distribution comparison between Freestream and S2-C with 5 μm uniform particles injection

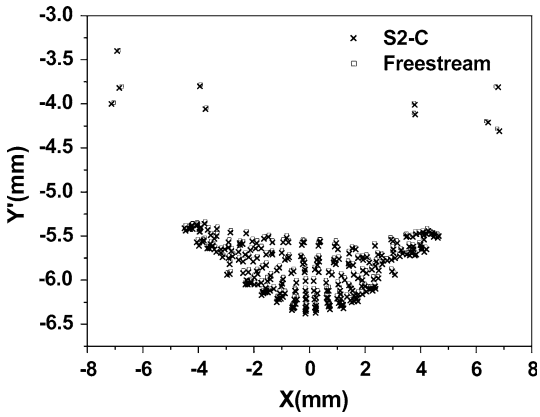

Fig. 24 Particle distribution comparison between Freestream and S2-C with 10 μm uniform particles injection

occurring with the mass transfer between particle and plasma is neglected. Therefore, the convective heat transfer equals the energy increase of the particle, $Q_c = W_p$, that is,

$$m_p C_p \Delta T_p = h A_p (T_l - T_p) \quad \text{(Eq 21)}$$

where Q_c and W_p are the convective heat transfer between plasma and particle and the energy increase of the particle, respectively. T_l and T_p are the temperature of plasma and particle, respectively, ΔT_p is the temperature variance of the particle, $\Delta T_p = T_p - T_i$, T_i is the initial particle temperature. By substituting the expressions of mass of the particle $m_p = 1/6\ \pi \rho_p D_p^3$, and the surface area $A_p = \pi D_p^2$, an equation of the particle temperature variance is derived:

$$\Delta T_p = \frac{6h}{(\rho_p D_p + 6h)(T_l - T_i)} \quad \text{(Eq 22)}$$

Therefore, the smaller particle has the tendency to acquire a higher temperature variance. In other words, the smaller particle experiences larger volumetric heat transfer because of their larger volumetric surface area.

In Fig. 27, light gray color scattered points represent each individual particle. The uppermost particles align in a nearly straight line, where the temperature reaches the boiling point and never goes up further. It is noted that some of the particles with relatively small sizes have lower temperature. This phenomenon may be understood by considering: the small particles have lower initial momentum when they flush into the nozzle; therefore they are unable to penetrate into the jet core, where the highest plasma temperature exists. In addition, the smaller particles cool down faster at the lower temperature regions of the plasma plume.

In this particle heat transport model, it is assumed that the Biot number is low ($\ll 1.0$), which means the particles have a nearly infinite thermal conduction. The instantaneous heat flow from the surface to the center of the particles gives it the uniform particle temperature. This

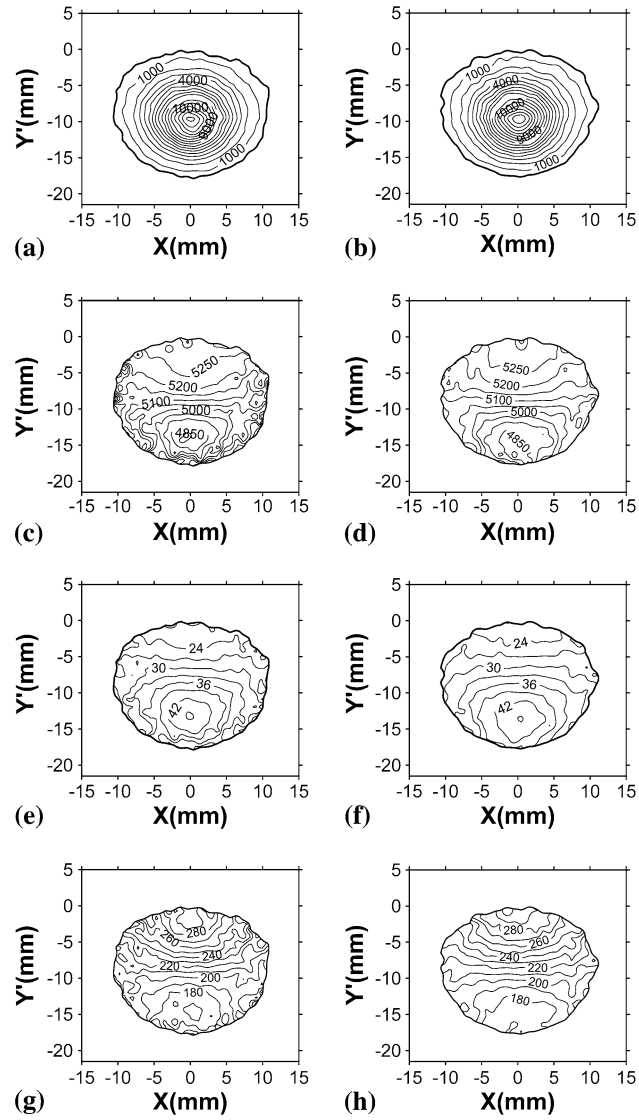

Fig. 25 Comparison of contours of particle in-flight parameters for S2-C case and the corresponding Freestream case. (a) Number contour in S2-C case. (b) Number contour in Freestream case. (c) Temperature contour in S2-C case. (d) Temperature contour in Freestream case. (e) Diameter contour in S2-C case. (f) Diameter contour in Freestream case. (g) Velocity contour in S2-C case. (h) Velocity contour in Freestream case

assumption is more suitable for metallic particles, which have much larger thermal conduction coefficient than zirconia. However, there are approximately 1 million particles being injected in this study, and it is not computationally feasible to consider internal conduction for every individual particle. Also, the intention of this study is to investigate the particle trajectories in the presence of substrates in the midst of the flow field. Therefore, an infinitely conductive model is sufficient.

Zirconia particles have poor heat conducting materials, which will result in a significant difference between the surface temperature and the internal temperature. In some cases, even when the surface temperature reach the

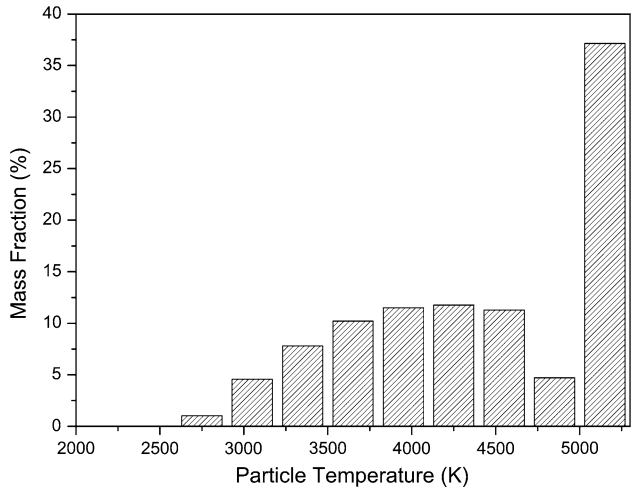

Fig. 26 Particle mass fraction distribution over different temperature ranges

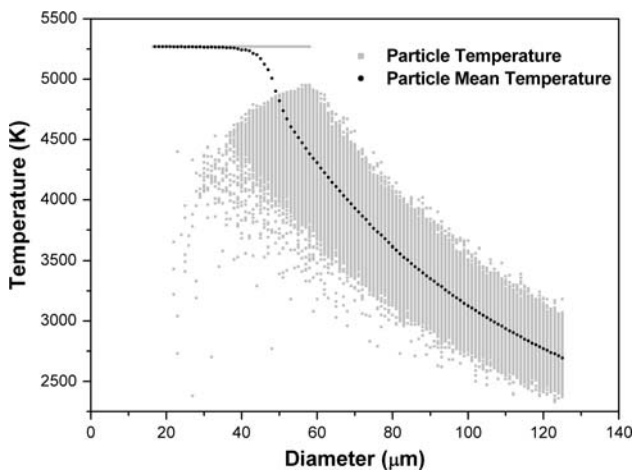

Fig. 27 Particle temperature and mean temperature distribution over diameter

boiling point, its center may still be in solid state (Ref 22). Therefore, particles will start evaporating earlier than the simulation data, which results in more severe mass losses. So the distribution of particle diameter will drift toward the smaller value, further making the particles more susceptible to the flow change by the substrate. However, even though the internal conduction is considered, the conclusion that the substrate inclusion has an insignificant effect on the particle in-flight parameters should also be valid, because of the small portion of the smaller particles and the relatively large initial size range (22 to 125 μm). Furthermore, the mass losses resulting from the evaporation (mentioned previously), together with the particle rebound and overspray at substrate, may be the dominant reasons for the rather low deposition efficiency (~40%) (Ref 15) in the actual spraying process using the same operating conditions.

4. Conclusions

In this work, a numerical model has been developed to investigate the effects of inclusion of curved-shaped substrate on the plasma flow fields and in-flight particle behavior. Under the combination of operating parameters used in our work, the inclusion of the substrate and also its dimensional shape and orientation influence the flow fields: the plasma plume in the most upper stream region remains unaffected until a short distance before the substrate (along the centerline). Substrate orientation (concave and convex) and dimensional shape (radius and substrate width) affect the flow behavior in a rather complicated way. When the substrate is large enough and in a concave orientation (as S2-C case), the flow is reversed in a bow shape. Plasma velocity is more affected by the substrate obstruction than the temperature.

Zirconia particles with different sizes are injected with different injection types (which is impossible in reality) to investigate the size effect on the particle trajectory and in-flight particle parameters along the trajectories. Smaller particles tend to acquire a higher velocity and temperature compared with their larger counterparts; however, some small particles cannot penetrate the plasma jet core region, resulting in a relatively low temperature. In addition, smaller particles are more susceptible to the diverging flow caused by the inclusion of the substrate. There exists a threshold size, above which there is no significant effect of the flow change on the particle trajectory. For the commercial zirconia particles we use in later work, the inclusion of substrate has nearly no effect on the particle spatial distribution and corresponding particle parameters. This finding supports the practice of using the Freestream case to model most types of plasma spray processing parameters.

References

1. M. Suarez, S. Bellayer, M. Traisnel, W. Gonzalez, D. Chicot, J. Lesage, E.S. Puchi-Cabrera, and M.H. Staia, Corrosion Behavior of Cr3C2-NiCr Vacuum Plasma Sprayed Coatings, *Surf. Coat. Technol.*, 2008, **202**(18), p 4566-4571
2. P. Fauchais, A. Vardelle, and B. Dussoubs, Quo Vadis Thermal Spraying?, *J. Therm. Spray Technol.*, 2001, **10**(1), p 44-66
3. K.A. Khor and Y.W. Gu, Thermal Properties of Plasma-Sprayed Functionally Graded Thermal Barrier Coatings, *Thin Solid Films*, 2000, **372**(1-2), p 104-113
4. R. Dal Maschio, V. Sglavo, L. Mattivi, L. Bertamini, and S. Sturlese, Indentation Method for Fracture Resistance Determination of Metal/Ceramic Interfaces in Thick TBCs, *J. Therm. Spray Technol.*, 1994, **3**(1), p 51-56
5. M. Vardelle, A. Vardelle, and P. Fauchais, Spray Parameters and Particle Behavior Relationships During Plasma Spraying, *J. Therm. Spray Technol.*, 1993, **2**(1), p 79-91
6. W. Zhang, L. Zheng, H. Zhang, and S. Sampath, Study of Injection Angle and Carrier Gas Flow Rate Effects on Particles In-Flight Characteristics in Plasma Spray Process: Modeling and Experiments, *Plasma Chem. Plasma Process.*, 2007, **27**(6), p 701-716
7. P.C. Huang, J. Heberlein, and E. Pfender, Particle Behavior in a Two-Fluid Turbulent Plasma Jet, *Surf. Coat. Technol.*, 1995, **73**(3), p 142-151

8. M.A. Jog and L. Huang, Transient Heating and Melting of Particles in Plasma Spray Coating Process, *J. Heat Transfer*, 1996, **118**(2), p 471-477
9. W. Wang, D. Li, J. Hu, Y. Peng, Y. Zhang, and D. Li, Numerical Simulation of Fluid Flow and Heat Transfer in a Plasma Spray Gun, *Int. J. Adv. Manufact. Technol.*, 2005, **26**(5), p 537-543
10. R. Westhoff, G. Trapaga, and J. Szekely, Plasma-Particle Interactions in Plasma Spraying Systems, *Metall. Mater. Trans. B*, 1992, **23**(6), p 683-693
11. R.L. Williamson, J.R. Fincke, and C.H. Chang, A Computational Examination of the Sources of Statistical Variance in Particle Parameters During Thermal Plasma Spraying, *Plasma Chem. Plasma Process.*, 2000, **20**(3), p 299-324
12. H. Martin, P.H. James, and T.F. Irvine, Jr., *Heat and Mass Transfer Between Impinging Gas Jets and Solid Surfaces. Advances in Heat Transfer*, Elsevier, Amsterdam, 1977, p 1-60
13. T.-C. Jen, L. Li, W. Cui, Q. Chen, and X. Zhang, Numerical Investigations on Cold Gas Dynamic Spray Process with Nano- and Microsize Particles, *Int. J. Heat Mass Transfer*, 2005, **48**(21-22), p 4384-4396
14. B. Samareh and A. Dolatabadi, A Three-Dimensional Analysis of the Cold Spray Process: The Effects of Substrate Location and Shape, *J. Therm. Spray Technol.*, 2007, **16**(5), p 634-642
15. C. Kang, H. Ng, and S. Yu, Comparative Study of Plasma Spray Flow Fields and Particle Behavior Near to Flat Inclined Substrates, *Plasma Chem. Plasma Process.*, 2006, **26**(2), p 149-175
16. M.I. Boulos, P. Fauchais, and E. Pfender, *Thermal Plasmas: Fundamentals and Applications*, 2nd ed., Plenum Publishing, New York, 1994
17. C.B. Ang, A. Devasenapathi, H.W. Ng, S.C.M. Yu, and Y.C. Lam, A Proposed Process Control Chart for DC Plasma Spraying Process. Part II. Experimental Verification for Spraying Alumina, *Plasma Chem. Plasma Process.*, 2001, **21**(3), p 401-420
18. B.E. Launder and D.B. Spalding, The Numerical Computation of Turbulent Flows, *Comput. Meth. Appl. Mech. Eng.*, 1974, **3**(2), p 269-289
19. *Fluent 6.1 User's Guide*, Fluent, Inc., 2003, p 10-49
20. C.L.V. Jayatilleke, The Influence of Prandtl Number and Surface Roughness on the Resistance of the Laminar Sublayer to Momentum and Heat Transfer, *Prog. Heat Mass Transfer*, 1969, **1**, p 193-329
21. S.A. Morsi and A.J. Alexander, An Investigation of Particle Trajectories in Two-Phase Flow Systems, *J. Fluid Mech. Digital Arch.*, 1972, **55**(02), p 193-208
22. E. Bourdin, P. Fauchais, and M. Boulos, Transient Heat Conduction Under Plasma Conditions, *Int. J. Heat Mass Transfer*, 1983, **26**(4), p 567-582
23. W.E. Ranz and W.R. Marshall, Evaporation from Drops, *Chem. Eng. Prog.*, 1952, **3**, p 141-146
24. J.W. McKelliget, G. Trapaga, E. Gutierrez-Miravete, and M. Cybulski, An Integrated Mathematical Model of the Plasma Spraying Processes, *Thermal Spray: Meeting the Challenges of the 21st Century*, C. Coddet Ed., ASM International, 1998, p 335-340
25. R. Bolot, J. Li, and C. Coddet, Some Key Advice for the Modeling of Plasma Jets Using FLUENT, *Thermal Spray 2005: Thermal Spray Connects: Explore Its Surfacing Potential*, E. Lugscheider, Ed., ASM International, 2005, p 1367-1371